Supplementary Information

Structure of the Catalytically Active Copper–Ceria Interfacial Perimeter

Aling Chen,[1†] Xiaojuan Yu,[2†] Yan Zhou,[1]* Shu Miao,[1] Yong Li,[1] Sebastian Kuld,[3] Jens Sehested,[3]* Jingyue Liu,[4] Toshihiro Aoki,[5] Song Hong,[6] Matteo Farnesi Camellone,[7] Stefano Fabris,[7] Jing Ning,[1] Chuanchuan Jin,[1] Chengwu Yang,[2] Alexei Nefedov,[2] Christof Wöll,[2] Yuemin Wang,[2]* Wenjie Shen[1]*

[1]State Key Laboratory of Catalysis, Dalian Institute of Chemical Physics, Chinese Academy of Sciences, Dalian 116023, China.

[2]Institute of Functional Interfaces, Karlsruhe Institute of Technology, Eggenstein-Leopoldshafen 76344, Germany.

[3]Haldor Topsøe A/S, Haldor Topsøes Allé 1, DK-2800 Kgs. Lyngby, Denmark.

[4]Department of Physics, Arizona State University, Tempe, Arizona 85287, USA.

[5]LeRoy Eyring Center for Solid State Science, Arizona State University, Tempe, Arizona 85287, USA.

[6]Center for Instrumental Analysis, Beijing University of Chemical Technology, Beijing 100029, China.

[7]Istituto Officina dei Materiali, Consiglio Nazionale delle Ricerche CNR-IOM, I-34149 Trieste, Italy.

[†]These authors contributed equally to this work.

*To whom correspondence should be addressed.

E-mail: zhouyan@dicp.ac.cn; jss@topsoe.dk; yuemin.wang@kit.edu; shen98@dicp.ac.cn

This file includes:

Supplementary Methods

Catalyst preparation

The Cu/CeO_2 catalysts were prepared by a multi-step process. First, the rod-shaped CeO_2 support was synthesized using a hydrothermal method, as we previously described[1]. To summarize, 5.2 g $Ce(NO_3)_3 \cdot 6H_2O$ was dissolved into 10 mL water and mixed with 40 mL 10 M NaOH aqueous solution at room temperature. The slurry was transferred to a 100 mL Teflon-lined stainless-steel autoclave, heated to 373 K and kept at that temperature for 20 h. The precipitate was collected by filtration, washed thoroughly with water and ethanol, dried at 353 K under vacuum overnight, and finally calcined at 773 K for 4 h in air. Then, the CuO/CeO_2 sample was prepared using a deposition-precipitation method. 2.0 g rod-shaped CeO_2 were dispersed into 10 mL aqueous solution containing 0.3 g $Cu(NO_3)_2 \cdot 3H_2O$ at room temperature. 40 mL 7.5 M NaOH aqueous solution was added dropwise into the slurry, and the mixture was heated to 353 K and held at that temperature for 20 h. The solid was collected by filtration, washed thoroughly with water and ethanol, dried at 353 K under vacuum overnight, and calcined at 573 K for 3 h in air. Finally, the Cu/CeO_2 catalysts were obtained by hydrogen (2.0 vol.% H_2/Ar) reduction of the CuO/CeO_2 precursor at 473-773 K for 2 h (heated to the desired temperature at a rate of 1 K min^{-1}); they were labeled as Cu-T, where T refers to the temperature of hydrogen reduction. Elemental analysis, which was performed by an inductively coupled plasma atomic emission spectroscopy (ICPS-8100), identified that the loading of copper in the Cu/CeO_2 catalysts was 3.36 wt.%.

Catalyst characterizations

The nitrogen adsorption-desorption isotherms were recorded on a Quantachrome NovaWin2 instrument at 77 K. Before the measurement, the sample was degassed at 573 K for 3 h. The surface area was calculated by a multipoint BET analysis of the adsorption isotherm.

The powder X-ray diffraction (XRD) patterns were recorded on a Rigaku diffractometer (D/Max-2500/PC) that operated at 40 kV and 200 mA using a Cu-Kα radiation source. The mean crystallite size of ceria was estimated from the half-width of the (111) diffraction line using the Scherrer's equation. The cell parameters were estimated from the diffraction lines within the 2theta degree of 20-80, using a whole pattern fitting and Rietveld refinement. The

temperature-programmed reduction by hydrogen (H_2-TPR) of the CuO/CeO_2 precursor was conducted with an Autochem II 2920 (Micromeritics). 100 mg CuO/CeO_2 sample (40–60 mesh) was loaded into a U-type quartz reactor (6 mm, inner diameter) and pretreated with a 20.0 vol.% O_2/N_2 mixture (30 mL min^{-1}) at 573 K for 1 h. After being cooled down to room temperature under Ar flow (30 mL min^{-1}), the sample was exposed to a 5.0 vol.% H_2/N_2 mixture (30 mL min^{-1}) and heated to 773 K at a rate of 10 K min^{-1}. The amount of consumed hydrogen was analyzed with a thermal conductivity detector.

The IR spectra were recorded on a state-of-the-art ultrahigh vacuum (UHV) apparatus, combing a FTIR spectrometer (Bruker Vertex 80v) and a multi-chamber UHV system (Prevac). This dedicated design not only allows to perform infrared reflection-absorption spectroscopy measurements at grazing incidence on well-defined model oxide surfaces, but also enables to record IR spectra in the transmission mode on polycrystalline oxide powders[2]. 200 mg CuO/CeO_2 sample was pressed into an inert metal mesh and mounted on a sample holder, which was specially designed for the transmission model IR measurements. The CuO/CeO_2 precursor was pretreated with O_2 at 573 K for 1 h to remove any surface impurities, and then reduced by H_2 at 473-773 K, resulting in the Cu-T catalysts. Exposure to CO, O_2 and D_2O at desired temperatures, typically 80-110 K, was achieved using a leak-valve-based directional doser connected to a tube (2 mm, inner diameter) that terminated 3 cm from the sample surface and 50 cm from the hot-cathode ionization gauge. The Cu/CeO_2 sample was exposed to CO at 80 K, and then heated to higher temperatures with a constant rate of 0.05 K s^{-1}, and the *in-situ* IR spectra were recorded continually. IR data were accumulated by recording 1024 scans with a resolution of 4 cm^{-1}. Before each exposure, a spectrum of the clean sample was recorded as a background reference. The binding energies of CO bound to the oxide-support and the metal were estimated from the temperature-dependent FTIR spectra, and a pre-exponential factor of 10^{13} s^{-1} was assumed[3]. The normalized peak areas were shown as a function of temperature.

The X-ray photoelectron spectra (XPS) were recorded on an Omicron Sphera II hemispherical XPS instrument using a monochromatic Al Kα source. The CuO/CeO_2 precursor was pressed into a thin disc and mounted onto a sample rod that placed in the pretreatment chamber

and was pretreated with a 20 vol.%O_2/N_2 (30 mL min^{-1}) mixture at 573 K for 1 h. It was then transferred into the analysis chamber, and the spectra of Cu2p, CuL_3VV, Ce3d, and O1s were recorded. Thereafter, the sample was reduced with a 5.0 vol.% H_2/Ar (30 mL min^{-1}) mixture at 473-773 K for 2 h at the pretreatment chamber, and the XPS of Cu2p, CuL3VV, Ce3d, and O1s in the Cu-T catalysts were recorded in the analysis chamber. Charging effect was corrected by adjusting the binding energy of Ce3d (v_0) to 882.5 eV.

The aberration-corrected high-angle annular dark-field (HAADF) scanning transmission electron microscopy (STEM) images and the electron energy loss spectroscopy (EELS) spectra for the CuO/CeO_2 precursor and the Cu-T catalysts were taken on a NION STEM100 at 60 kV, which was equipped with monochromator, aberration corrector, and Gatan Enfinium spectrometer. This STEM-EELS combination allows atomic image as well as atomic chemical information, with the spatial resolution < 0.1 nm and the energy resolution < 15 meV. The width and the thickness of CuO and/or Cu clusters were estimated from the STEM images, based on the value of the line intensity profile across the entire cluster. The standard deviations for the width and the thickness of the copper clusters were 0.07 and 0.03 nm, respectively, by measuring the same clusters for 20 times. The probe size used in EELS experiments was about 0.1 nm, and a short acquisition time of 2 s was adapted; line-scanning EELS were recorded with a spatial step of < 0.11 nm and spectral dispersion of 0.1 eV or 0.8 eV per pixel with a typical dwell time of 1.5 s. The collector angle for HAADF images was 70~200 mrad, with a probe convergence angle of ~30 mrad; EELS collection semi-angle was 45 mrad using a 3 mm entrance aperture. The atom-resolved HAADF-STEM images of the copper clusters and the copper-ceria interfaces in the Cu-T samples were recorded on a JEOL ARM200F microscope (cold-field emission) operated at 200 kV. The collector angle for HAADF images was 68~280 mrad with a probe convergence semi-angle of 24 mrad. The specimen was prepared by ultrasonically dispersing the sample in ethanol, and droplets of the suspensions were deposited onto lacey carbon-coated copper or gold grids and dried in air. To avoid the electron beam irradiation, low dose rate was adapted to obtain the HAADF images and expose the sample to the electron beam only during the image acquisition process. The average size of the copper clusters in the respect Cu-T catalyst was estimated by counting about 100 clusters that were unambiguously verified by STEM and EELS. The deviation for measuring the distances of the adjoining atomic columns in copper clusters and at the copper-cerium in the HAADF-STEM images was 0.01 nm.

DFT calculations

The spin-polarized density functional theory (DFT) calculations employed the Perdew-Burke-Ernzerhof generalized gradient-corrected approximation for the exchange and correlation functional[4]. A Hubbard U term added to the PBE energy functional (DFT+U)[5] and acting on the Ce4f orbitals allowed for an accurate description of the electronic structure of both oxidized and reduced ceria systems[6]. The value of the parameter U was set to 4.5 eV. The interaction between valence electrons and ions was described with Vanderbilt ultrasoft pseudo potentials[7]. The electron wave function and the augmentation charge density were expanded on a plane-wave basis set limited by energy cut-off of 30 Ry and 300 Ry, respectively. All the calculations employed periodic boundary conditions and were performed with the Quantum Espresso package[8].

Catalytic test

The low-temperature water-gas shift (WGS) reaction was performed with a continuous-flow fixed-bed quartz tubular reactor (6 mm, inner diameter) under atmospheric pressure. 100 mg CuO/CeO_2 (40–60 mesh) was diluted with 200 mg quartz sand and placed between two layers of quartz wools inside the reactor. The sample was heated from room temperature to 573 K at a rate of 5 K min^{-1} and kept at that temperature for 1 h by flowing a 20.0 vol.% O_2/N_2 mixture (30 mL min^{-1}) to remove any surface impurities. After being cooled down to room temperature under Ar flow (30 mL min^{-1}), the sample was reduced with a 2.0 vol.% H_2/Ar mixture (30 mL min^{-1}) by raising the temperature at a rate of 1 K min^{-1} to the desired values (473-773 K) and kept at that temperature for 2 h. As the temperature was set at 473 K, the feed gas of 1.0 vol.% CO/3.0 vol.% H_2O/He (67 mL min^{-1}) was introduced into the reactor, and the reaction was tested for about 10 h. The effluent from the reactor was analyzed online with a gas chromatography equipped with a thermal conductivity detector and a flame ionization detector. To accurately determine the concentrations of CO and CO_2 in the outlet gases, a nickel catalyst converter, used for converting CO and CO_2 into methane, was placed before the flame ionization detector. For kinetic study, the conversion of CO was adjusted to be around 10% by varying the flow rate of the reaction gas or the weight of the catalyst, and thus the reaction rate was measured at a differential reactor condition.

Supplementary Discussion

Structure of the CuO/CeO_2 precursor

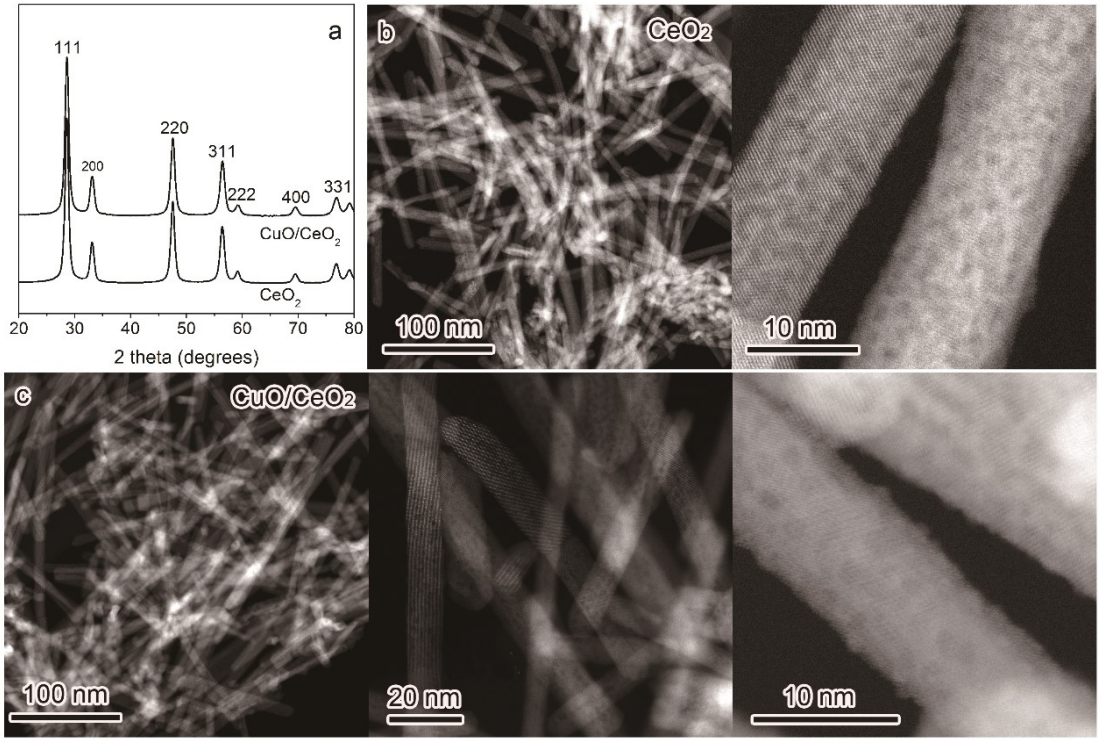

Supplementary Figure 1. XRD patterns (**a**) and HAADF-STEM images (**b,c**) of the rod-shaped CeO_2 support (**b**) and the CuO/CeO_2 precursor (**c**).

Supplementary Table 1. Structure properties of the CuO/CeO_2 precursor

Sample	CeO_2(111) plane		CeO_2 lattice constant (nm)	CeO_2 crystalline size (nm)	BET surface area ($m^2 g^{-1}$)
	2θ (°)	d (nm)			
CeO_2	28.573	3.1214	5.4086	12.0	104
CuO/CeO_2	28.584	3.1202	5.4071	11.1	93

The rod-shaped ceria support had a mean diameter of 10 nm and an average length of 80 nm, with a BET surface area of 104 $m^2 g^{-1}$ and a typical cubic fluorite structure (Supplementary Fig. 1a,b and Table 1). The CuO/CeO_2 sample showed distinct diffraction lines of ceria, while the diffraction of the typical (111) line slightly shifted to a higher 2 theta. This indicates the incorporation of Cu^{2+} into ceria lattice, forming surface-substituted Cu-O_x-Ce solid solution. Since the radius of Cu^{2+} (0.072 nm) is smaller than that of Ce^{4+} (0.092 nm), its incorporation into ceria slightly decreases the lattice constant and forms O vacancies[9-11]. The CuO/CeO_2 sample had almost the same size as the rod-shaped ceria support; CuO clusters were dispersed on the surface of ceria rods (Supplementary Fig. 1c).

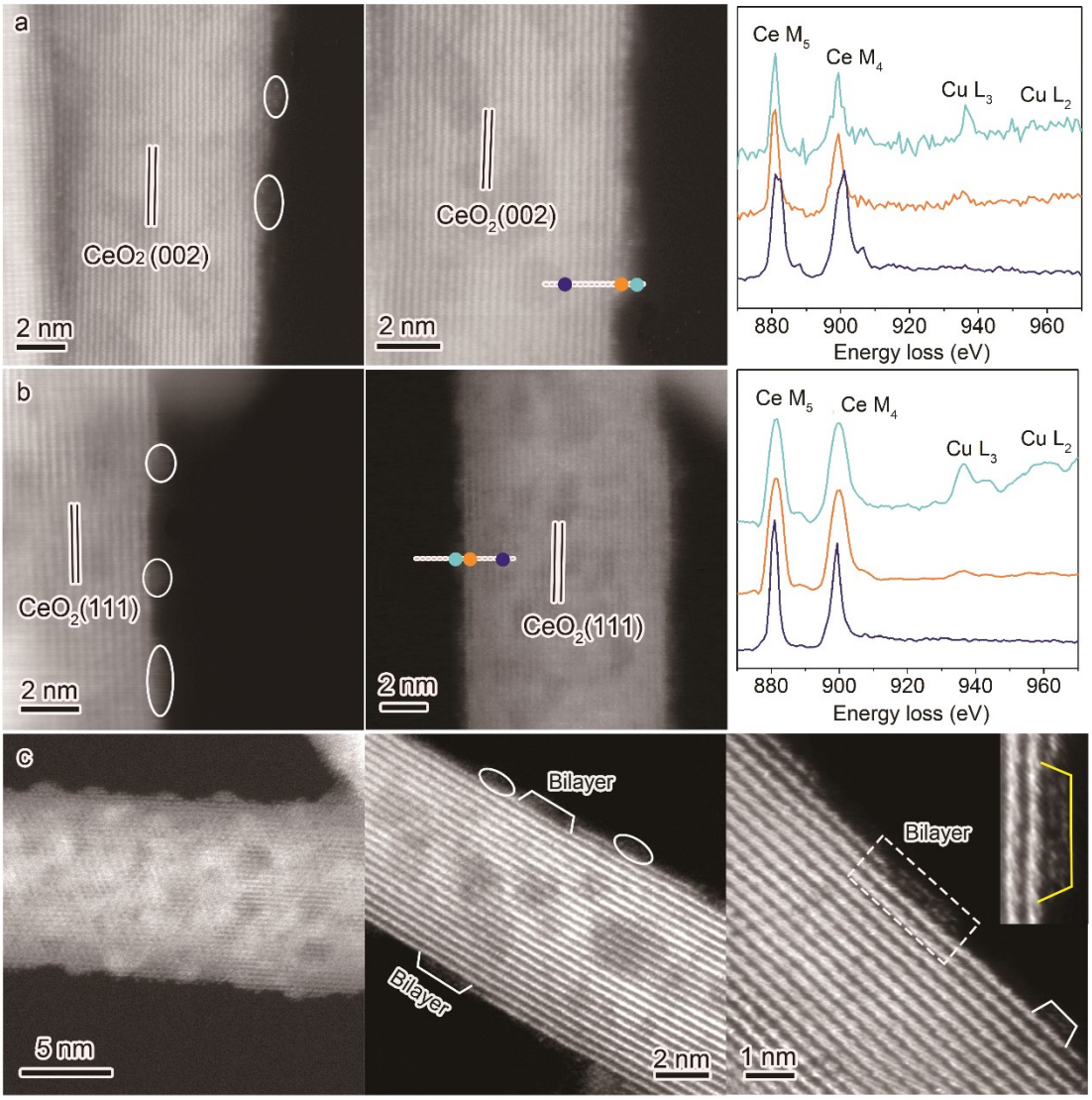

Supplementary Figure 2. HAADF-STEM images of CuO clusters dispersed on CeO_2(100) **(a)** and (111) **(b)** facets; line-scanning EELS (right-side) correspond to the spatial distributions of copper and cerium from the top surface of an individual copper cluster to the central area of ceria rod, marked with cyan, orange and navy spots in **a** and **b**; the intensity ratios of the Ce $M_{4,5}$ edges in the EELS in **a** indicate the dominant presence of Ce^{3+} species around and/or near the CuO clusters, while these of the Cu $L_{2,3}$ edges confirm the Cu^{2+} species. Atom-resolved HAADF-STEM images of CuO clusters on ceria rods **(c)**, showing CuO domains, monolayers and bilayers on ceria rods; the inset is an enlarged image of a selected area, showing the arrangement of copper atoms within a bilayered CuO cluster.

Detailed STEM analysis verified that CuO clusters of 1.3 nm wide and 0.54 nm thick dominantly located on CeO_2(111) while smaller CuO clusters (~1.0 nm) mainly populated on CeO_2 (100) (Supplementary Fig. 2a,b), showing a facet-dependent deposition of CuO on ceria. The smaller CuO clusters might be caused by the stronger interaction between copper oxide

and the (100) facet of ceria[12]. EELS analysis resolved the chemical environment of CuO on ceria. The sharp peaks at 930-950 eV are generally attributed to Cu $L_{2,3}$ edges; while the peak at 936 eV (i.e. the white line), which is characteristic of electron removal from the d band *via* charge transfer (ionic bonding), indicates Cu^{2+} species[13]. The chemical state of cerium could be judged from the intensity ratio (I_{M5}/I_{M4}) of Ce $M_{4,5}$ edges, which is 1.31 for Ce^{3+} and 0.91 for Ce^{4+} species[14]. Line-scanning EELS of Ce $M_{4,5}$ edges across the CuO cluster on CeO_2(100) surface showed a gradual decrease in the I_{M5}/I_{M4} ratio from the CuO-CeO_2 boundary (1.26) to the central area of ceria rod (~2 nm away from the interface, 0.97), suggesting the abundance of Ce^{3+} at the CuO-CeO_2 interface and the dominant presence of Ce^{4+} on the bulk CeO_2 rod. Atom-resolved HAADF-STEM images showed that copper oxide domains (only few copper atoms), monolayers and bilayers preferentially anchored at the step edges of ceria rods, and their contact sites with ceria surface were clearly resolved (Supplementary Fig. 2c). Statistics on about 100 CuO clusters, which could be unambitiously identified by STEM and EELS, verified that most CuO clusters presented as a bilayer structure: the bottom copper layer was connected with the top layer of cerium atoms on ceria rods *via* interfacial oxygen atoms (invisible in HAADF).

Hydrogen reduction of the CuO/CeO_2 precursor

Reduction of the CuO/CeO_2 precursor by H_2 occurred mainly at 383-493 K; there were two partially overlapped reduction peaks at 443 and 473 K, respectively. The first peak was assigned to the reduction of finely dispersed CuO; while the second intense peak consisted of the reduction of surface-substituted Cu-O_x-Ce solid solution and the accompanied reduction of ceria surface[9,12,15]. The minor peak at 513 K, together with the weak reduction at high temperatures, standed for the further reduction of ceria. Because the total amount of hydrogen consumed by these characteristic reductions (1005 $\mu mol \cdot g^{-1}$) was much greater than the stoichiometric value (529 $\mu mol \cdot g^{-1}$) for the transformation of CuO to Cu, partial reduction of ceria occurred simultaneously. This indicates a synergetic interaction between CuO and CeO_2 during the reduction process; the initial reduction of the finely dispersed CuO formed metallic copper (Cu^0), which substantially promoted the followed reductions of the Cu-O_x-Ce solid solution and the surface oxygen on ceria *via* a hydrogen spillover effect[12,15].

Most likely, the Cu-O_x-Ce solid solution, which is located either at the bottom layer of the CuO clusters or directly at the surface of ceria as domains/monolayers, was transformed into the interfacial copper species [12].

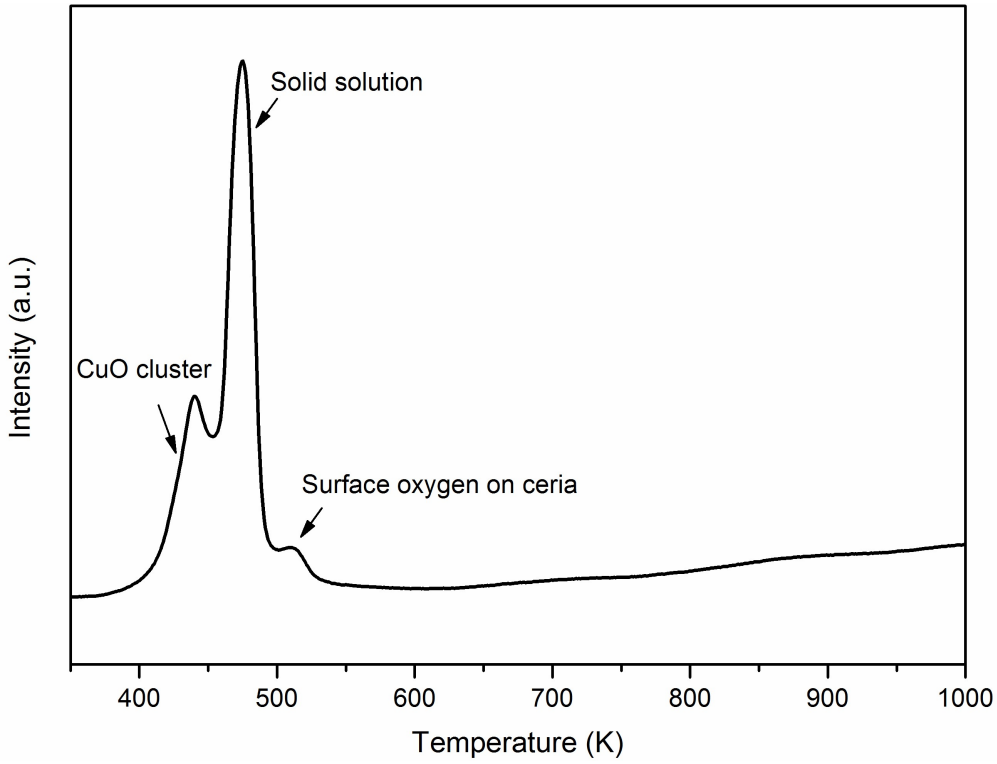

Supplementary Figure 3. H_2-TPR profile of the CuO/CeO_2 precursor.

STEM images and EELS of the Cu/CeO_2 catalysts

On the Cu-473 sample, copper domains, monolayers and bilayers were all observed on the ceria surface, where the bilayers dominantly presented with a mean width of ~1.0 nm and an average thickness of ~0.40 nm (Supplementary Fig. 4a,b). Line-scanning EELS of Cu $L_{2,3}$ edges crossing an individual copper cluster verified that copper spatially distributed from the top edge of the cluster to the copper-ceria interface; the bulk area of the cluster was mainly metallic while the Cu-CeO_2 interface consisted of partially oxidized copper species, as evidenced by the variations in the shapes of the $L_{2,3}$ edges (Supplementary Fig. 4c). Judged from the relative intensity (I_{M5}/I_{M4}) ratio of Ce $M_{4,5}$ edges, which slightly decreased from 1.23 at the interface to 1.20 on the ceria rod (~1.5 nm away from the interface), Ce^{3+} species were relatively dominant around the Cu clusters. Atom-resolved HAADF-STEM images showed that copper monolayers and bilayers preferentially anchored at the step edges of ceria rods, and their contact sites with ceria surfaces were clearly resolved (Supplementary Fig. 4d-f).

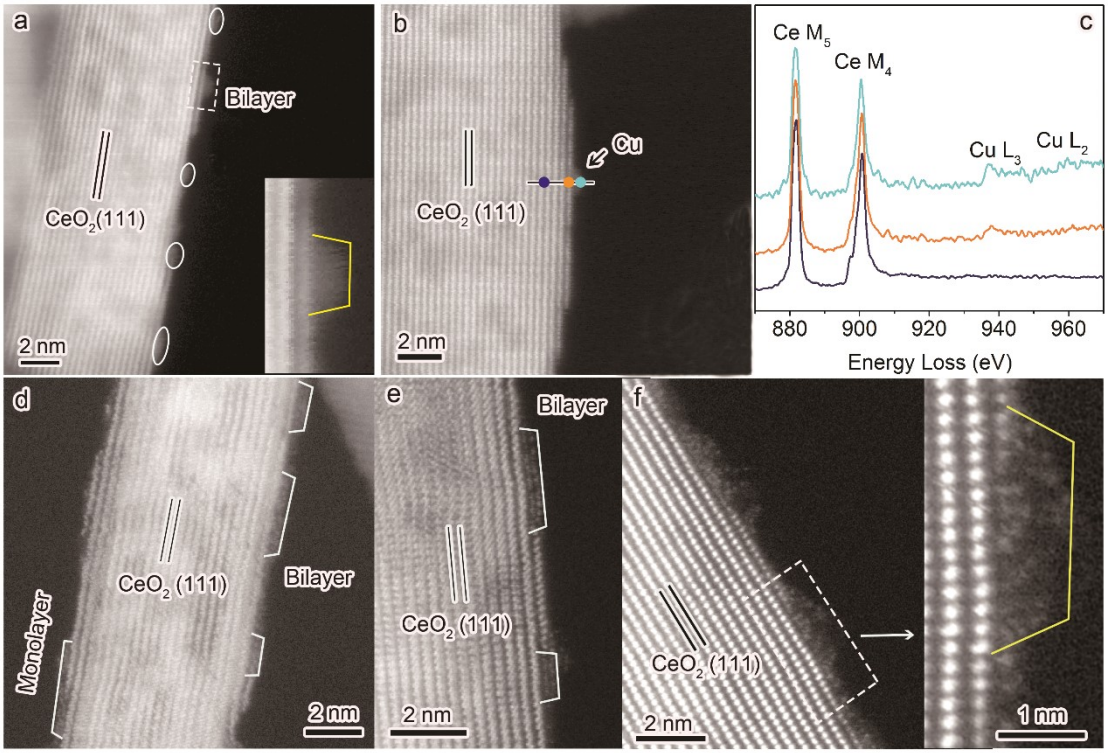

Supplementary Figure 4. HAADF-STEM images (**a,b**) and EELS (**c**) of the Cu-473 catalyst. The insert in (**a)** is an enlarged image of a copper cluster. The EELS spectra in **c** refer to a line-scanning from the topmost surface of an individual copper cluster to the central area of ceria rod, indicated with cyan, orange and navy spots in **b,** verifying the spatial distribution and the chemical state of copper and cerium species. Atom-resolved HAADF-STEM images (**d-f**) of Cu monolayers and bilayers on ceria rods; the inset in **f** is an enlarged image of the selected area, showing the geometric arrangement of copper atoms within a copper cluster.

As increasing the temperature during hydrogen treatment, Cu clusters in the Cu-T catalysts slightly enlarged. The average width of the copper clusters gradually increased from 1.1 nm on Cu-573 to 1.2 nm on Cu-673 (Supplementary Fig. 5) and further to 1.5 nm on Cu-773 (Supplementary Fig. 6), while the mean thickness kept at 0.40-0.46 nm that approximately equals to a bilayer configuration. This clearly indicates a rather strong chemical bonding between the copper clusters and the ceria support even at 773 K under hydrogen. Again, line-scanning EELS of Cu $L_{2,3}$ crossing typical Cu clusters on the Cu-573 and Cu-673 catalysts showed that the bulk area of the Cu cluster was metallic but the Cu-CeO_2 interface consisted of metallic and positively-charged copper species (Supplementary Fig. 5). This could be identified from the shapes of the Cu $L_{2,3}$ edges; Cu^0 is characterized by flat and broad $L_{2,3}$ while partially oxidized copper is accompanied by a sharp L_3[13]. The corresponding spectra of Ce $M_{4,5}$ edges indicated that the I_{M5}/I_{M4} ratio at the Cu-CeO_2 interface (1.30) was apparently

higher than that on the central area of CeO_2 (1.23), suggesting a rich presence of Ce^{3+} at the interfaces[14]. Atom-resolved HAADF-STEM images on the Cu-773 sample verified that copper bilayers dominantly presented and preferentially located at the step edges of the ceria rods (Supplementary Fig. 6). The contact sites between copper atoms at the bottom layer and the cerium atoms (through oxygen atoms that are invisible in HAADF) were clearly identified.

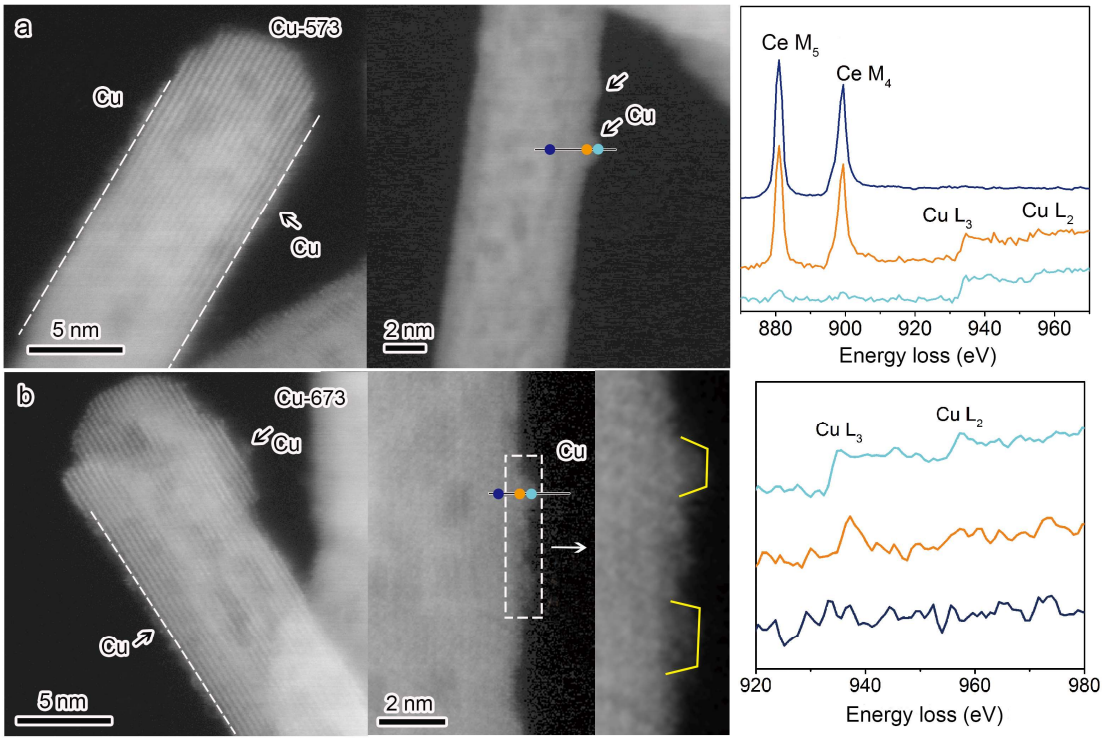

Supplementary Figure 5. Aberration corrected HAADF-STEM images and EELS of the Cu-573 (**a**) and Cu-673 (**b**) catalysts. The EELS (right-side) correspond to the line-scanning spectra of Ce $M_{4,5}$ and Cu $L_{2,3}$ edges crossing the copper clusters marked with cyan, orange and navy spots, respectively. The inset in **b** is an enlarged image of the rectangular area, showing the copper clusters.

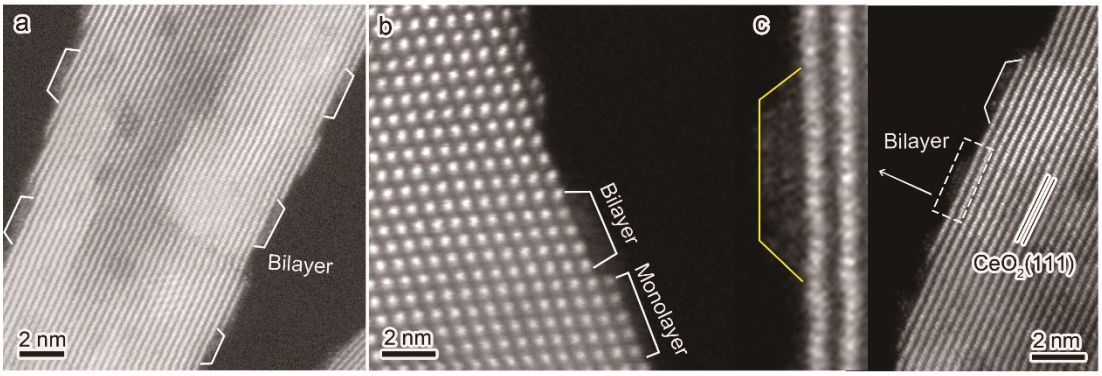

Supplementary Figure 6. Atom-resolved HAADF-STEM images of the Cu-773 catalyst. Copper monolayers, bilayers and trilayers were clearly seen; the inset in **c** is an enlarged image that shows the atomic arrangement in a typical copper bilayer that is dominantly presented in the sample.

Surface properties of the Cu/CeO_2 catalysts

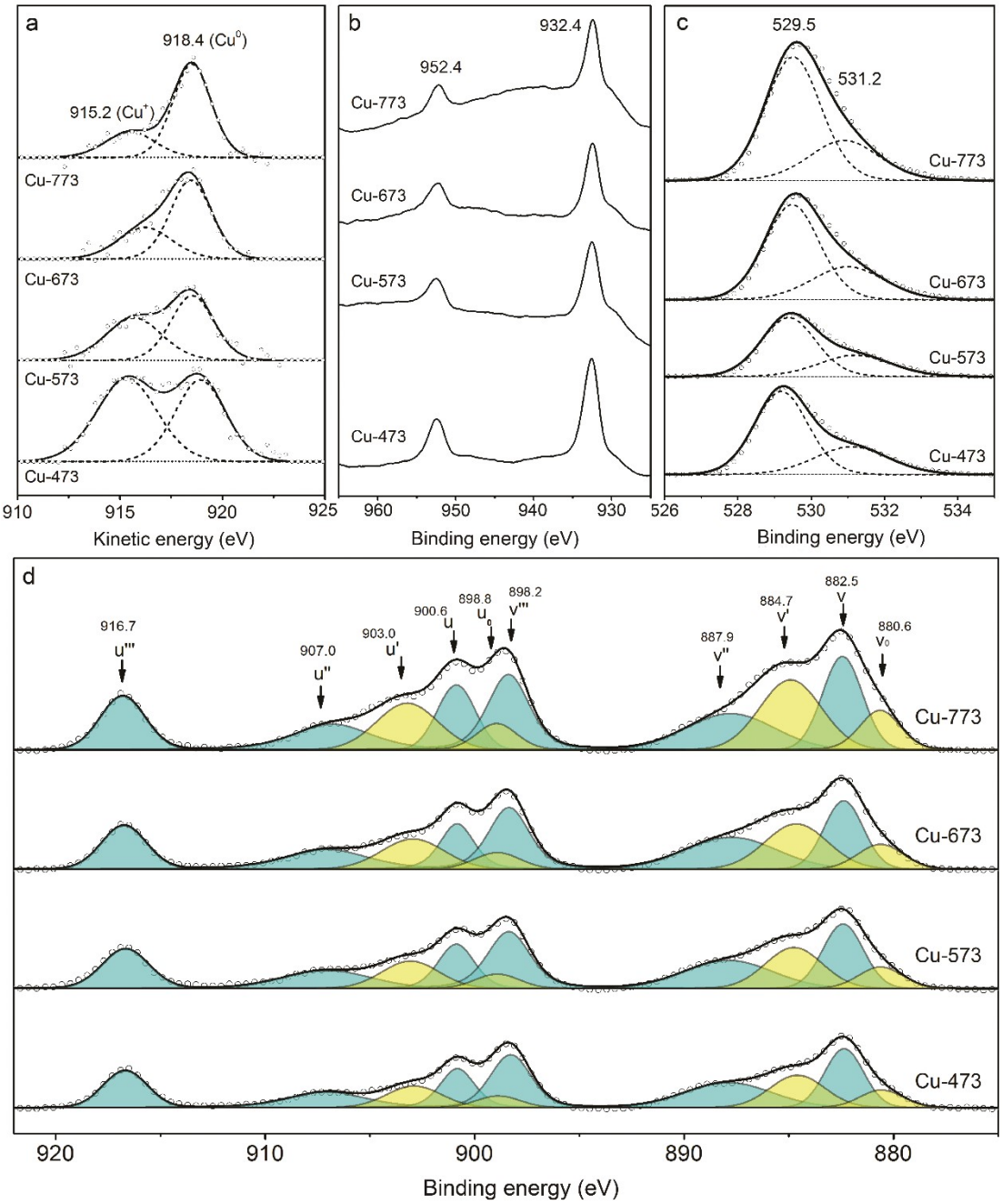

Supplementary Figure 7. XPS of CuL3VV (**a**), Cu2p (**b**), O1s (**c**) and Ce3d (**d**) in the Cu-T catalysts. The CuO/CeO_2 precursor was reduced with hydrogen at desired temperatures (473-773 K) for 2 h in a pretreatment chamber and the resulting Cu-T samples were directly transferred into the analysis chamber.

XPS analysis on the Cu-T catalysts verified the chemical states of copper, cerium and oxygen (Supplementary Fig. 7). The binding energy of $Cu2p_{3/2}$ at 932.4 eV generally indicated copper

species; the kinetic energy at 918.4 eV in CuL3VV Auger spectra represented Cu^0 species while that at 915.2 eV confirmed Cu^+ species[16], suggesting the co-existence of both Cu^0 and Cu^+ in the Cu-T samples. As increasing the temperature for hydrogen treatment, the intensities of the binding energy and the kinetic energy for Cu^0 enhanced but the intensity of the kinetic energy, representing Cu^+, weakened. Based on a semi-qualitative analysis of the XPS lines, the Cu^+/Cu^0 ratio was found to decrease sharply from 1.22 for Cu-473 to 0.85 on Cu-573, followed by a moderate decline to 0.36 on Cu-773 (Supplementary Table 2).

Supplementary Table 2. Surface atomic compositions of the Cu-T catalysts as determined by XPS

Sample	Surface atomic ratio (molar)		
	Cu^+/Cu^0	$O_{II}/(O_I + O_{II})$	$Ce^{3+}/(Ce^{3+} + Ce^{4+})$
CuO/CeO_2	---	0.13	0.08
Cu-473	1.22	0.32	0.27
Cu-573	0.85	0.32	0.29
Cu-673	0.52	0.31	0.32
Cu-773	0.36	0.29	0.36

The XPS of Ce3d consisted of two sets of spin-orbital multiplets of $Ce3d_{3/2}$ and $Ce3d_{5/2}$ contributions; the peaks labeled u′, v′, u^0, and v^0 referred to Ce^{3+} while the peaks labeled u′′′ and v′′′, u′′ and v′′, u, and v corresponded to Ce^{4+}. The concentration of surface Ce^{3+} was calculated from the relative intensities of the u_0 (v_0) and u′ (v′) peaks to the total intensity of Ce3d region[9,16]. For the CuO/CeO_2 precursor, the surface concentration of Ce^{3+} was only 8% (Supplementary Table 2), but it sharply increased to 27% in the Cu-473 sample, suggesting a substantial reduction of surface ceria, accompanied with the reduction of Cu^{2+} to Cu^0/Cu^+. As further raising the temperature, the proportion of surface Ce^{3+} only moderately enhanced to 29% for Cu-573, 32% for Cu-673 and 36% for Cu-773, indicating a gradual reduction of ceria.

The XPS of O1s contained two peaks; the major peak (O_I) with a binding energy at 529.5 eV was assigned to lattice oxygen while the minor peak (O_{II}) at 531.2 eV was associated with oxygen vacancies on the ceria[9,16]. The concentration of O_{II} was 32% on the Cu-473 sample, and it slightly decreased to 29% on the Cu-773 sample. This result indicates that hydrogen

reduction promoted the generation of surface oxygen vacancies, especially in the Cu-473 sample, while the slight decrease at higher temperatures might be caused by the replenishment of bulk oxygen to surface, involving the reduction of bulk ceria.

The chemical states of copper and cerium species in the Cu-T catalysts were also probed by temperature-programmed desorption of hydrogen (H_2-TPD) and N_2O reactive frontal chromatograph (N_2O-RFC). The CuO/CeO_2 precursor was reduced with a 3.0 vol.% H_2/He mixture by heating from room temperature to 473 or 773 K at a rate of 2 K min^{-1} and kept at that temperature for 2 h. Then, H_2-TPD and N_2O-RFC measurements were sequentially conducted. The H_2-TPD measurement exclusively detected surface Cu^0 species[17] while the N_2O-RFC titration probed both Cu^0 and Ce^{3+} species on the surface[18]. For the Cu-473 catalyst, the amount of Cu^0 was 54.24 µmol g^{-1}, calculated from the hydrogen capacity in the H_2-TPD profile (Supplementary Fig. 8a) by assuming a stoichiometry of $Cu^0/H = 1.5$[17,19]. The oxygen capacity, i.e. the sum of the uptakes from Ce^{3+} and Cu^0 during the N_2O-RFC titration (Supplementary Fig. 8b), was 213.9 µmol g^{-1}. Based on a stoichiometry of Cu^0/N_2O = $Ce^{3+}/N_2O = 2.0$[18], the amount of surface Ce^{3+} was estimated to be 373.6 µmol g^{-1}. On the Cu-773 catalyst, the amount of Cu^0 decreased to 23.0 µmol g^{-1} while the amount of surface Ce^{3+} increased to 434.1 µmol g^{-1} (Supplementary Table 3), confirming the generation of more oxygen vacancies and the growth of copper clusters. The large amount of Ce^{3+} species that are closely linked to the number of oxygen vacancies manifests that a substantial fraction of the catalyst surface is highly oxygen deficient. This is in excellent agreement with the XPS data presented above.

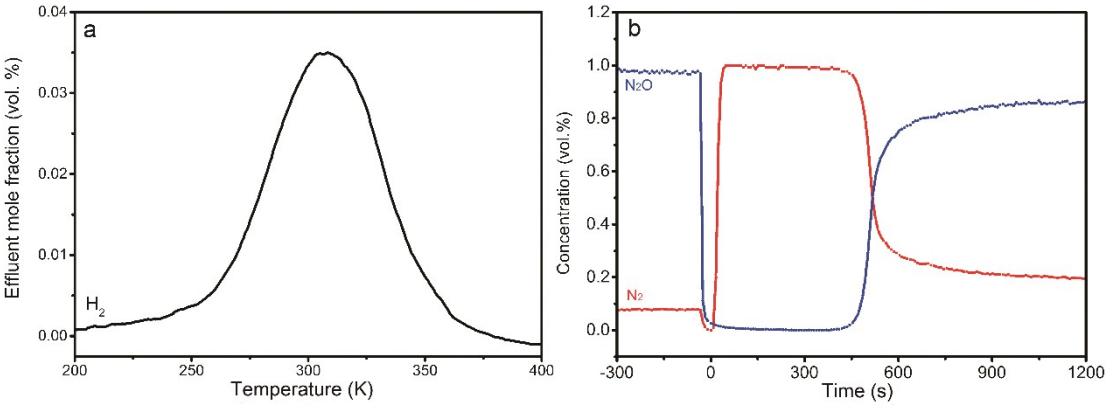

Supplementary Figure 8. H_2-TPD (**a**) and N_2O-RFC (**b**) profiles of the Cu-473 catalyst.

Supplementary Table 3. Total amounts of surface Cu^0 and Ce^{3+} on the Cu-T catalysts as determined by H_2-TPD/N_2O-RFC

Sample	H_2 capacity ($\mu mol\ g^{-1}$)	Oxygen capacity ($\mu mol(O)\ g^{-1}$)	Cu^0 ($\mu mol\ g^{-1}$)	Ce^{3+} ($\mu mol\ g^{-1}$)	Ce^{3+}/Cu^0
Cu-473	18.08	213.91	54.24	373.57	6.89
Cu-773	7.67	228.56	23.01	434.12	18.87

IR spectra of the Cu/CeO_2 catalyst

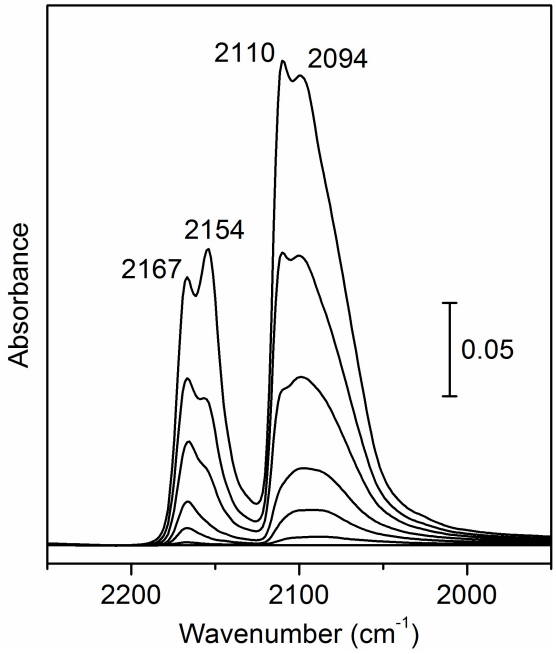

Supplementary Figure 9. IR spectra recorded upon exposing the Cu-473 catalyst to CO at 80 K and gradually increasing the pressure of CO from 1 x 10^{-5} to 1 x 10^{-2} mbar.

Upon exposure of the Cu-473 catalyst to CO and gradually increasing the pressure of CO, four IR bands were resolved at 2167, 2154, 2110 and 2094 cm^{-1}. The two high-frequency bands are characteristic for CO bound to ceria surfaces; the band at 2154 cm^{-1} was identified as CO weakly adsorbed on the Ce^{4+} site while the 2167 cm^{-1} band was assigned to CO bound to the defect sites[2]. The two low-frequency bands at 2110 and 2094 cm^{-1} originated from CO adsorbed on Cu^+ and Cu^0 sites[20], respectively. Note, the IR intensity of the CO-Cu bands was much higher than that of the ceria-related ones. This is because of the different types of interaction of CO with copper and ceria. The bonding of CO to the defect site on ceria is dominated by the weak electrostatic interaction (Stark effect), while CO adsorbs more

strongly on electron-rich Cu^+ and Cu^0 sites *via* π back-donation. Consequently, the transition dipole moment of the CO stretching vibration for CO-Cu^+ and CO-Cu^0 is substantially larger than that of CO bound to ceria, which accounts for the higher intensity observed for the copper-related CO bands.

Modelling of the copper-ceria interfaces

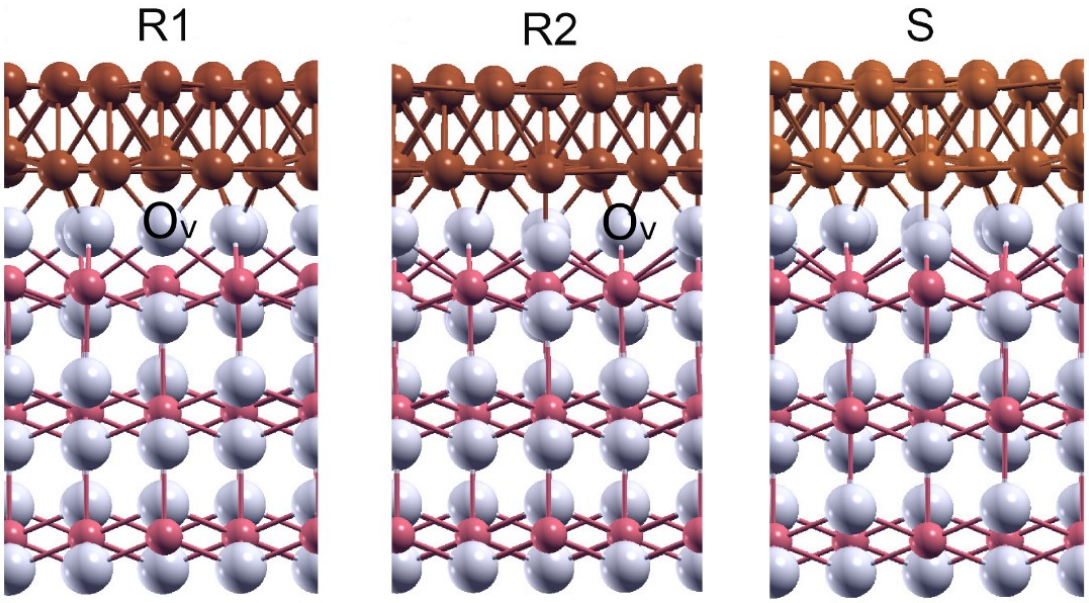

Supplementary Figure 10. Equilibrium structures of the Cu bilayer on the reduced (R1 and R2) and stoichiometric (S) CeO_2(111) surfaces. O_v marks the position of the oxygen vacancy. Color codes as in Fig. 4a.

Supplementary Table 4. Distances (Å) of the atomic planes (calculated as the average z coordinate of the atoms in each plane) from the interfacial plane of O atoms, which is taken as the origin.

	O	**Ce**	**O**	**O**	**Ce**	**O**	**O**	**Ce**	**O**	**Cu**	**Cu**
R1	-8.52	-7.73	-6.93	-5.38	-4.58	-3.79	-2.05	-1.37	0	1.61	3.67
R2	-8.44	-7.65	-6.85	-5.31	-4.50	-3.73	-2.01	-1.32	0	1.75	3.81
S	-8.52	-7.73	-6.93	-5.39	-4.58	-3.80	-2.10	-1.37	0	1.79	3.76

The copper-ceria interface was modelled with a periodic supercell slabs consisting of two Cu layers supported on three O-Ce-O trilayers and with a vacuum thickness of 20 Å along the z direction perpendicular to the Cu(111)/CeO_2(111) interface. Integrals in the Brillouin zone were performed on a Monkhorst-Pack (4x4x1) k-point mesh. A coherent (2x2)CeO_2/(3x3)Cu interface was generated by taking the equilibrium bulk lattice parameter for the ceria slab

and the in-plane lattice parameter for the Cu bilayer. All the atomic coordinates were optimized according to the Hellmann-Feynman forces except for the lowermost O-Ce-O trilayer that was constrained at its equilibrium coordinates.

The reduced ceria substrate was modelled by including O vacancies (O_v) at the Cu-CeO_2 interface with 0.25 ML coverage[6]. Two reduced ceria systems (labelled as R1 and R2), differing in the position of O_v, were considered. R1 is obtained by removing the O atom directly underneath an interfacial Cu atom while R2 is obtained by removing the O atom bridging between two Cu atoms at the interface. A reference stoichiometric interface (labelled as S) was also computed. The fully relaxed atomic structures of the R1, R2 and S systems are displayed in Supplementary Fig. 10, while the resulting interplanar distances are listed in Supplementary Table 4. The comparison between the ground-state total energies of the R1 and R2 supercells predicts that R1 is more stable than R2 by 0.5 eV, and therefore the manuscript reports the results obtained for the most stable R1 system.

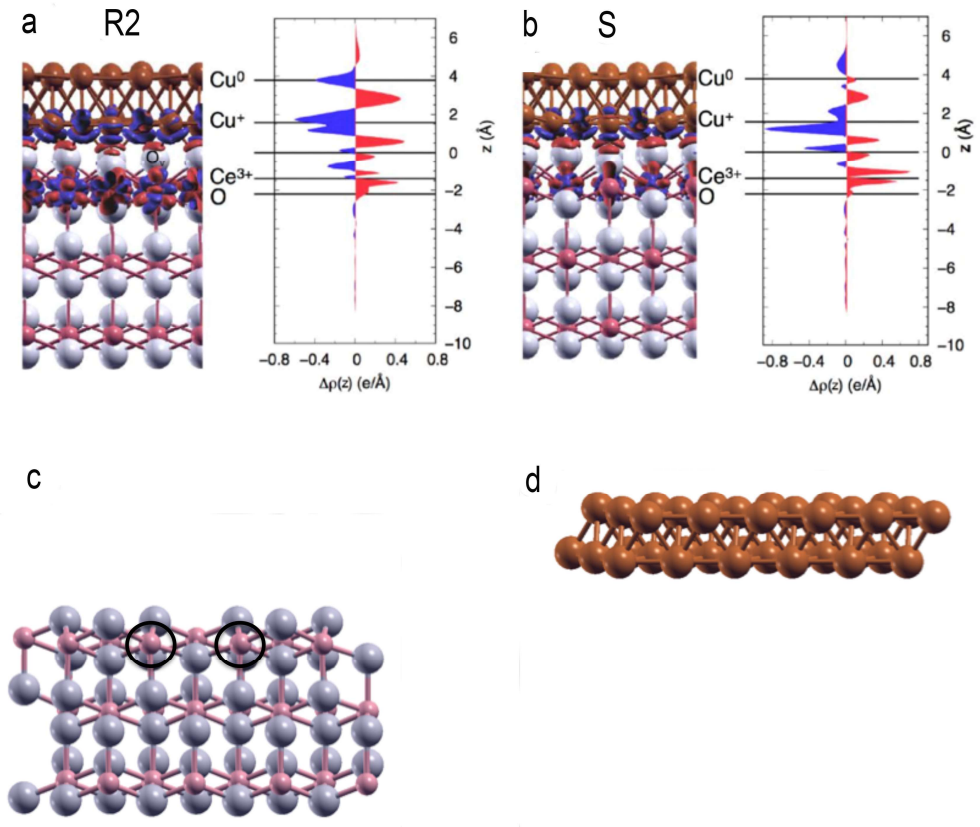

Supplementary Figure 11. Fully-relaxed structures of the R2 (**a**) and S (**b**) systems and calculated bonding charge Δρ(r) that corresponds to the plane-integrated bonding charge Δρ(z) across the interfaces. The red and blue areas represent charge accumulation and depletion, respectively. Color

codes as in Fig. 4a. **c**,**d** Reference auxiliary systems used in the calculation of the bonding charge Δρ(z) for the system R1; where the Ce^{3+} ions are marked by a black circle.

Supplementary Table 5. Calculated net Bader charges (e) for the 9 Cu atoms of the interfacial (Cu_I) layer in the Cu/CeO_2(111) supercells*.

		Cu_1	**Cu_2**	**Cu_3**	**Cu_4**	**Cu_5**	**Cu_6**	**Cu_7**	**Cu_8**	**Cu_9**
R1	**Cu_I**	-0.17	-0.15	-0.17	-0.20	-0.18	-0.18	-0.16	+0.02	+0.19
	Cu_{II}	+0.01	0.00	+0.02	0.00	0.00	+0.01	0.00	+0.02	+0.01
R2	**Cu_I**	+0.02	0.00	-0.20	+0.13	-0.09	-0.21	-0.22	-0.19	-0.29
	Cu_{II}	0.00	0.00	+0.02	+0.01	+0.02	0.00	0.00	+0.03	+0.02
S	**Cu_I**	-0.03	-0.21	-0.20	-0.21	-0.24	-0.22	-0.22	-0.20	+0.72
	Cu_{II}	0.00	-0.01	0.00	+0.01	0.00	+0.01	-0.01	+0.04	+0.02

*The Bader charges are reported as differences with respect to the charge of a neutral Cu atom (11.00).

The electronic characterization as well as the interfacial charge transfer are based on the calculation of the Bader charges of the bonding charge Δρ(**r**). Both quantities are obtained from the self-consistent ground state electron density of the complete system: $\rho_{Cu/sub}(\mathbf{r})$. In particular, the interfacial bonding charge Δρ(**r**) is defined as the difference between $\rho_{Cu/sub}(\mathbf{r})$ and the densities of the clean CeO_2(111) substrate, $\rho_{sub}(\mathbf{r})$ and of the free-standing metallic Cu bilayer, $\rho_{Cu}(\mathbf{r})$: $\Delta\rho(\mathbf{r}) = \rho_{Cu/sub}(\mathbf{r}) - \rho_{Cu}(\mathbf{r}) - \rho_{sub}(\mathbf{r})$. The reference substrate and free-standing Cu bilayer employed in the calculations of the most stable R1 configuration are reported in Supplementary Fig. 11. The bonding charge Δρ(**r**) as well as Δρ(z) obtained by integrating Δρ(r) over planes parallel to the R1, R2 and S interfaces are displayed in Supplementary Fig. 11 (the corresponding analysis for R1 is shown in Fig. 4b,c of the manuscript); the Bader charges calculated for all the Cu atoms in the interfacial and outermost layers, denoted as Cu_I and Cu_{II}, respectively, are summarized in Supplementary Table 5.

Both the Bader charges and bonding charge Δρ(z) analysis demonstrate that the outermost Cu atoms are metallic (net Bader charge ~0 e) while a charge depletion is displayed by several interfacial Cu atoms (net Bader charge ~ -0.2 e). As a reference for the Bader charge of a formal Cu^+, the value was calculated for bulk Cu_2O (~ -0.4 e). The interfacial charge

transfer from the Cu bilayer to the CeO_2(111) substrate leads to the reduction of all the Ce ions of the CeO_2 layer in contact with the Cu bilayer that formally change their oxidation state from Ce^{4+} to Ce^{3+}. The charge transfer is estimated on the basis of the different number of reduced Ce^{3+} induced by the contact with the Cu bilayer. As clearly shown by the bonding charge Δρ(z) analysis, this charge reorganization involves only the interface Cu atoms and the first (O,Ov) -Ce-O trilayer of the ceria substrate. The comparison between the R1, R2 and S systems shows that the charge transfer from the Cu bilayer to the substrate is more pronounced in the stoichiometric case than in the case of reduced substrates. This is further corroborated by the calculated Bader charges shown in Supplementary Table 5.

Reaction kinetics and active sites

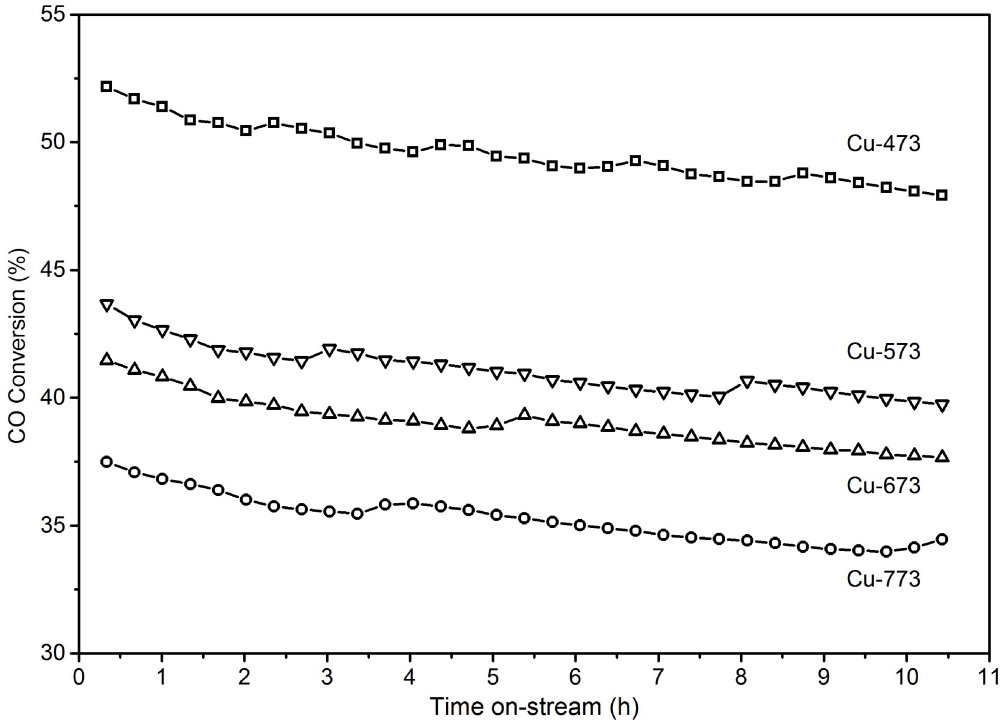

Supplementary Figure 12. Water-gas shift reaction over the Cu-T catalysts. The reaction was tested at 473 K with a feed gas of 1.0 vol.%CO/3.0 vol.%H_2O/He (40,000 mL $g_{cat.}^{-1}$ h^{-1}).

The average conversion of CO was ~50% on Cu-473 for the WGS reaction, and it gradually lowered to 35% over Cu-773 under the identical reaction conditions, primarily because of the increasing size of copper clusters in the Cu/CeO_2 catalysts (Supplementary Fig. 12). The reaction rate, measured under a differential reactor condition, enhanced as increasing the total length of the copper-ceria interfacial perimeter in the Cu-T catalysts (Supplementary

Table 6). A further correlation between the reaction rate and the number of Cu^+ atom located at the interfacial perimeter resulted in almost identical turnover frequencies (TOFs). This strongly suggests that the activity of the Cu-T catalysts for the low-temperature WGS reaction is intimately linked to the copper-ceria interfacial perimeter.

Supplementary Table 6. Reaction rates and turnover frequencies (TOFs) of the Cu-T catalysts

Sample	CO conversion (%)	Reaction rate ($mol_{CO}\ g_{Cu}^{-1}\ s^{-1}$)	Perimeter length ($m\ g_{cat.}^{-1}$)	Number of perimeter Cu^+ atom	TOF (s^{-1})
Cu-473	10.7	1.47×10^{-4}	3.7×10^{10}	1.18×10^{20}	2.47×10^{-2}
Cu-573	9.3	1.29×10^{-4}	3.5×10^{10}	1.11×10^{20}	2.78×10^{-2}
Cu-673	10.2	1.18×10^{-4}	3.2×10^{10}	1.02×10^{20}	2.84×10^{-2}
Cu-773	8.9	0.95×10^{-4}	2.3×10^{10}	0.73×10^{20}	2.56×10^{-2}

The total length of the copper-ceria interfacial perimeter and the number of perimeter Cu^+ site for the respect Cu-T catalyst were calculated from the average size of copper clusters that was determined by STEM analysis. The total number of Cu clusters was derived from the content of copper (3.36 wt.%) and the average sizes of the copper clusters in the respect catalyst. Reaction conditions: 473 K, 1.0 vol.% CO/3.0 vol.% H_2O/He, 321,600-398,019 mL· $g_{cat.}^{-1}\ h^{-1}$.

FTIR measurements demonstrated that the activation of water occurred exclusively at the oxygen vacancies on the ceria surface. As exposing the Cu/CeO_2 catalyst to water (D_2O) at 250 K, the major band at 2693 cm^{-1}, which is characteristic for hydroxyl (OD) groups on the ceria surface[2], indicated the dissociative adsorption of water (Supplementary Fig. 13). The shoulder band at 2714 cm^{-1}, which is accompanied by a rather broad feature between 2630 and 2200 cm^{-1}, are typical for H-bonds[2]. This confirms the coexistence of molecular and dissociated water species on the Cu-473 catalyst. It has been experimentally demonstrated that on the stoichiometric ceria (111) surface, water adsorbs molecularly at Ce^{4+} sites without dissociation[21-23]. Furthermore, DFT calculations have predicted that the intact water molecules are bound to substrate O atoms *via* H-bonding[24-26]. Temperature-dependent IR spectra revealed that the hydroxyl (OD) band, formed by water dissociation on the oxygen vacancies, kept unchanged up to 450 K, whereas the IR signals for H-bonds decreased gradually as raising the temperature. This provides direct evidence for the activation of water at the oxygen vacancies on the ceria surface, forming hydroxyl groups.

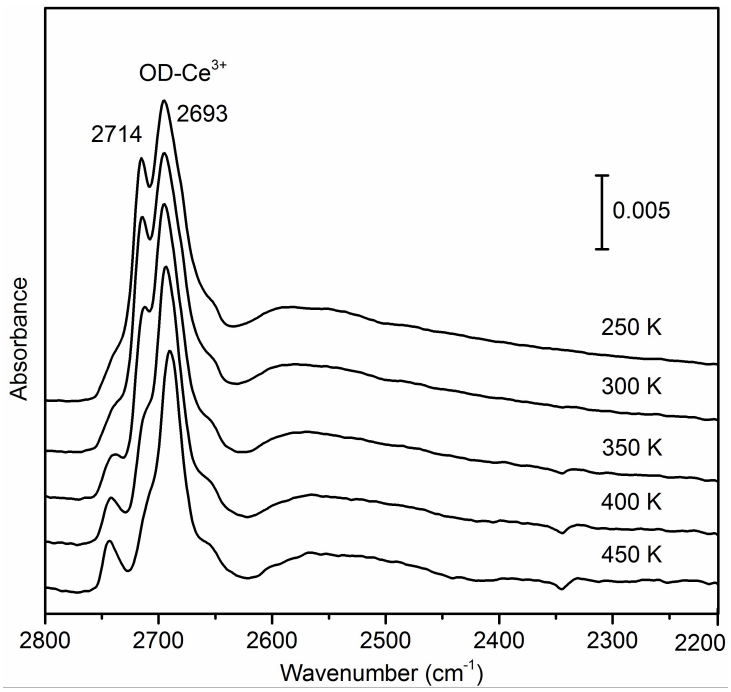

Supplementary Figure 13. IR spectra recorded after exposing the Cu-473 catalyst to D_2O at 250 K and heating to 450 K gradually.

Supplementary References

1. Chen, A., Zhou, Y., Ta, N., Li, Y. & Shen, W. Redox properties and catalytic performance of ceria–zirconia nanorods. *Catal. Sci. Technol.* **5**, 4184−4192 (2015).
2. Wang, Y. & Wöll, C. IR spectroscopic investigations of chemical and photochemical reactions on metal oxides: bridging the materials gap. *Chem. Soc. Rev.* **46**, 1876−1932 (2017).
3. Redhead, P. A. Thermal desorption of gases. *Vacuum* **12**, 203−211 (1962).
4. Perdew, J. P., Burke, K. & Ernzerhof, M. Generalized gradient approximation made simple. *Phys. Rev. Lett.* **77**, 3865 (1996).
5. Cococcioni, M. & de Gironcoli, S. Linear response approach to the calculation of the effective interaction parameters in the LDA+U method, *Phys. Rev. B* **71**, 035105 (2005).
6. Fabris, S., Vicario, G., Balducci, G., de Gironcoli, S. & Baroni, S. Electronic and atomistic structures of clean and reduced ceria surfaces. *J. Phys. Chem. B* **109**, 22860−22867 (2005).
7. Vanderbilt, D. Soft self-consistent pseudopotentials in a generalized eigenvalue formalism. *Phys. Rev. B* **41**, 7892 (1990).
8. Giannozzi, P. et al. QUANTUM ESPRESSO: a modular and open-source software project for quantum simulations of materials. *J. Phys.: Condens. Matter* **21**, 395502 (2009).
9. Shan, W. J., Shen, W. & Li, C. Structural characteristics and redox behaviors of $Ce_{1-x}Cu_xO_y$ solid

solutions. *Chem. Mater.* **15**, 4761−4767 (2003).

10. Wang, X. et al. Unusual physical and chemical properties of Cu in $Ce_{1-x}Cu_xO_2$ oxides. *J. Phys. Chem. B* **109,** 19595−9603 (2005).
11. Elias, J. S. et al. Elucidating the nature of the active phase in copper/ceria catalysts for CO oxidation. *ACS Catal.* **6,** 1675–1679 (2016).
12. Wang, W. et al. Crystal plane effect of ceria on supported copper oxide cluster catalyst for CO oxidation: importance of metal–support Interaction. *ACS Catal.* **7,** 1313–1329 (2017).
13. Keast, V. J., Scott, A. J., Brydson R., Williams, D. B. & Bruley, J. Electron energy-loss near-edge structure-a tool for the investigation of electronic structure on the nanometre scale. *J. Microsc.* **203**, 135−175 (2001).
14. Wu, L. et al. Oxidation state and lattice expansion of CeO_{2-x} nanoparticles as a function of particle size. *Phys. Rev. B* **69**, 125415 (2004).
15. Tang, X. et al. CuO/CeO_2 catalysts: redox features and catalytic behaviors. *Appl. Catal. A: Gen.* **288**, 116−125 (2005).
16. Tschöpe, A., Trudeau, M. L. & Ying, J. Y. Redox properties of nanocrystalline Cu-doped cerium oxide studied by isothermal gravimetric analysis and X-ray photoelectron spectroscopy. *J. Phys. Chem. B* **103**, 8858−8863 (1999).
17. Kuld, S., Conradsen, C., Moses, P. G., Chorkendorff, I. & Sehested, J. Quantification of zinc atoms in a surface alloy on copper in an industrial-type methanol synthesis catalyst. *Angew. Chem. Int. Ed.* **53**, 5141−5145 (2014).
18. Tschöpe, A., Markmann, J., Zimmer, P. & Birringer, R. N_2O temperature-programmed oxidation and EXAFS studies on the dispersion of copper in ceria-supported nanocatalysts. *Chem. Mater.* **17**, 3935−3943 (2005).
19. Fichtl, M. B. et al. Counting of oxygen defects versus metal surface sites in methanol synthesis catalysts by different probe molecules. *Angew. Chem. Int. Ed.* **53**, 7043–7047 (2014).
20. Martínez-Arias, A., Fernández-García, M., Soria, J. & Conesa, J. C. Spectroscopic study of a Cu/CeO_2 catalyst subjected to redox treatments in carbon monoxide and oxygen. *J. Catal.* **182**, 367−377 (1999).
21. Gritschneder, S. & Reichling, M. Structural elements of CeO_2 (111) surfaces. *Nanotechnology* **18**, 044024 (2007).
22. Gritschneder, S., Iwasawa, Y. & Reichling, M. Strong adhesion of water to CeO_2 (111).

Nanotechnology **18**, 044025 (2007).

23. Lykhach, Y. et al., Water chemistry on model ceria and Pt/Ceria catalysts. *J. Phys. Chem. C* **116**, 12103–12113 (2012).
24. Kumar, S. & Schelling, P. K. Density functional theory study of water adsorption at reduced and stoichiometric ceria (111) surfaces. *J. Chem. Phys*. **125**, 204704 (2006).
25. Fronzi, M., Piccinin, S., Delley, B., Traversa, E. & Stampfl, C. Water adsorption on the stoichiometric and reduced CeO_2 (111) surface: a first-principles investigation. *Phys. Chem. Chem. Phys*. **11**, 9188−9199 (2009).
26. Yang, Z., Wang, Q., Wei, S., Ma, D. & Sun, Q. The effect of environment on the reaction of water on the ceria (111) surface: A DFT+U study. *J. Phys. Chem. C* **114**, 14891–14899 (2010).